On Stretching, Bending, Shearing, and Twisting of Actin Filaments I: Variational Models

Carlos Floyd, Haoran Ni, Ravinda S. Gunaratne, Radek Erban,* and Garegin A. Papoian*

Cite This: *J. Chem. Theory Comput.* 2022, 18, 4865−4878

Read Online

ACCESS | Metrics & More | Article Recommendations | Supporting Information

ABSTRACT: Mechanochemical simulations of actomyosin networks are traditionally based on one-dimensional models of actin filaments having zero width. Here, and in the follow up paper (*arXiv*, DOI 10.48550/arXiv.2203.01284), approaches are presented for more efficient modeling that incorporates stretching, shearing, and twisting of actin filaments. Our modeling of a semiflexible filament with a small but finite width is based on the Cosserat theory of elastic rods, which allows for six degrees of freedom at every point on the filament's backbone. In the variational models presented in this paper, a small and discrete set of parameters is used to describe a smooth filament shape having all degrees of freedom allowed in the Cosserat theory. Two main approaches are introduced: one where polynomial spline functions describe the filament's configuration, and one in which geodesic curves in the space of the configurational degrees of freedom are used. We find that in the latter representation the strain energy function can be calculated without resorting to a small-angle expansion, so it can describe arbitrarily large filament deformations without systematic error. These approaches are validated by a dynamical model of a Cosserat filament, which can be further extended by using multiresolution methods to allow more detailed monomer-based resolution in certain parts of the actin filament, as introduced in the follow up paper. The presented framework is illustrated by showing how torsional compliance in a finite-width filament can induce broken chiral symmetry in the structure of a cross-linked bundle.

Efficiently represent geometry of finite-width filaments

Model collective chiral mechanics of many filaments
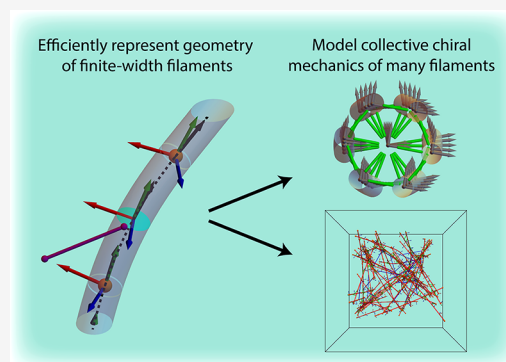
1. INTRODUCTION

Simulations of the actin-based cytoskeleton allow for deep insights into its dynamics and mechanical properties. Composed primarily of cross-linked actin filaments and molecular motors, this structural protein network exhibits fascinating behaviors on a range of spatial scales.[2,3] From the ångström scale, at which individual actin monomers and molecular motors hydrolyze chemical fuel to drive conformational changes, up to the millimeter scale, at which collectives of cells exert self-organized mutual forces on one another, the nonequilibrium dynamics and mechanics of cytoskeletal networks enable much of the cellular functionality necessary for life.[4−11] Associated with this wide range of spatial scales is a variety of computational techniques that are used for modeling cytoskeletal networks.[12] Each technique accounts to some level of approximation for the mechanical and geometrical properties of actin filaments. These filaments can be classified as semiflexible polymers (whose typical contour lengths are comparable to their persistence length) with very large aspect ratios (such that the contour length is much greater than the filament's radius).[13,14] In this paper, we will focus on network-level computational models of cytoskeletal systems, which typically assign ~10−100 monomers to a single discrete computational element. Software packages such as AFiNeS,[15] CytoSim,[16] the model of Kim and co-workers,[17] and

MEDYAN[18] can access time scales of thousands of seconds and length scales of tens of micrometers, allowing exploration of fascinating emergent phenomena of cytoskeletal systems which comprise many interacting filaments. In the coarse-grained mechanical models used in these platforms, an actin filament is represented as a one-dimensional piecewise-linear chain of elastic segments with stretching and bending energy penalties. An effective radius can be assigned to the filament so that it experiences excluded volume interactions with its neighbors to prevent overlap, but the elastic strain energy functions used in these models neglect the filament width.[19]

There is strong reason to expect that the finite width of an actin filament, neglected in current network-level models of cytoskeletal systems, plays an important role in cytoskeletal dynamics. Experiments *in vivo* and *in vitro* have illustrated the emergence of remarkable rotating dynamical phases of cytoskeletal systems, in which vortex structures spontaneously
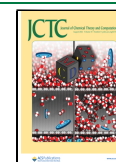
emerge as a broken chiral symmetry of the system.[20−22] These collective rotating phases likely involve torques exerted about the axes of the actin filaments, which should have chirally asymmetric torsional compliances due to the filaments' helical microstructure.[23,24] The resulting "twirling" of actin filaments by myosin motors has been directly observed *in vitro*.[25,26] Furthermore, these torques have been argued to have developmental consequences by contributing to left−right symmetry breaking in the cell cortex.[27,28] However, the intrinsic chirality and torque generation in actin filaments is not captured in any existing cellular scale mechanochemical models of cytoskeletal networks, which currently do not allow for torques or shearing forces due to their one-dimensional filament representations. Other computational studies also highlight the importance of filament torsion in cytoskeletal assemblies.[29−31] Although these latter studies have implemented models of filament mechanics that include torsional deformations, either the corresponding strain energy functions are overly simple and do not systematically account for all allowable modes of deformation (stretching, bending, shearing, and twisting), or else the models are too computationally expensive to use in network-level simulations of cytoskeletal networks, where collective phenomena involving many filaments are observed.[29−31] Further efforts in modeling actomyosin networks described in refs 32 and 33, do account for the finite width of actin filaments, but they are limited by large computational expense, an overly simplified set of possible chemical reactions (which excludes active myosin motor walking and filament polymerization), and no option for binding of cross-linkers to the filament surface rather than its backbone. As a result, the question remains open of how one can incorporate all allowable mechanical deformations of a finite-width filament network in a highly efficient way, so that the model can be used in cellular scale mechanochemical simulation packages such as MEDYAN.[18]

Here, we introduce a set of options for efficiently modeling a semiflexible filament having a small but finite width. The physical background used in these models is the Cosserat theory of elastic rods, which allows for six degrees of freedom at every point on the filament's backbone.[34,35] A key feature of these modeling approaches is that they use only a small, discrete set of model parameters yet describe a smooth filament shape having all allowable degrees of freedom in the Cosserat theory. We present two main approaches: one in which polynomial spline functions are used to describe the positional and orientational degrees of freedom, and one in which we use the geodesic curve in the space of the orientational degrees of freedom. We find that in the latter model one can calculate the strain energy function without resorting to a small-angle expansion, so it can describe arbitrarily large filament deformations without systematic error. In section 2, we first introduce the relevant ingredients from the Cosserat theory used in our work, after which we introduce two new filament models and describe how to calculate the strain energy function in each. In section 3, we then validate these models by comparing them with computationally expensive but higher resolution Cosserat filament.[36] We apply our new method to illustrate how chiral torsional compliance in a finite-width filament can propagate up a spatial scale to induce broken chiral symmetry in the structure of a cross-linked bundle. Finally, we implement these new models into MEDYAN to illustrate the feasibility of using them to study network-level cytoskeletal systems.

2. METHODS

Thin rods (or filaments) are characterized by large aspect ratios, allowing for an effectively one-dimensional continuum mechanical description where position in the rod is specified with a single variable.[37,38] Several nonlinear theories of thin rod mechanics have been developed which differ from each other in the allowed types of deformations. The Cosserat theory[34,35] generalizes the Kirchoff theory[39,40] by allowing for transverse shearing and axial extension deformations. Here we build on the Cosserat theory, which has recently been used to develop mathematical models of thin rod dynamics that capture a wide range of observed nonlinear filament behaviors.[36,41,42] We next give a brief account of aspects of the Cosserat theory relevant to our model, after which we describe our new variational treatment.

2.1. Background of Cosserat Theory. In the Cosserat theory, a filament is mathematically described by a directed curve.[34,43] This consists of backbone curve $r(\hat{s}) \in \mathbb{R}^3$, where $\hat{s} \in [0,\hat{L}]$ is the reference arc-length coordinate, and an orthonormal triad of directors $\boldsymbol{D}(\hat{s}) = (\boldsymbol{d}_1(\hat{s}), \boldsymbol{d}_2(\hat{s}), \boldsymbol{d}_3(\hat{s}))$. In our notation the caret hat symbol denotes a variable of the reference configuration. The column vectors $\boldsymbol{d}_\alpha(\hat{s}) \in \mathbb{R}^3$, where $\alpha = 1, 2, 3$ indexes the Cartesian components, specify the orientation of the rod's cross-section at $\hat{s}$ is specified such that $\boldsymbol{d}_3(\hat{s})$ is normal to the cross-section and $\boldsymbol{d}_1(\hat{s})$ and $\boldsymbol{d}_2(\hat{s})$ span the cross-section and define its twist about $\boldsymbol{d}_3(\hat{s})$. These vectors generally differ from the Frenet-Serret frame comprising the tangent, normal, and binormal vectors of $r(\hat{s})$.[44] We distinguish between the current configuration of the rod, described by $r(\hat{s})$ and $\boldsymbol{D}(\hat{s})$, and the reference (undeformed) configuration, described by a reference curve $\hat{r}(\hat{s})$ and a reference triad $\hat{\boldsymbol{D}}(\hat{s}) = (\hat{\boldsymbol{d}}_1(\hat{s}), \hat{\boldsymbol{d}}_2(\hat{s}), \hat{\boldsymbol{d}}_3(\hat{s}))$. Dilatation of the rod's backbone length is captured by the scalar quantity $e(\hat{s}) = \mathrm{d}s/\mathrm{d}\hat{s}$, which can be used to change coordinates from the reference arc-length coordinate $\hat{s}$ to the current arc-length coordinate s. In this paper we primarily use the reference coordinate system, although our formulation is equivalent to one using the current coordinate system. The proper orthogonal rotation $\boldsymbol{Q}(\hat{s}) \in \mathbb{R}^{3 \times 3}$ rotates the reference triad into the current one:

$$\boldsymbol{D}(\hat{s}) = \boldsymbol{Q}(\hat{s})\hat{\boldsymbol{D}}(\hat{s}) \tag{1}$$

In what follows, we will assume $\hat{\boldsymbol{D}}$ is independent of $\hat{s}$ for simplicity. The quantities just introduced are illustrated in Figure 1.

From these quantities, six independent components of strain are defined.[37,38] Three of these components are encoded in the pseudovector

$$\boldsymbol{\kappa} = \mathrm{ax}\left(\boldsymbol{Q}^{\mathrm{T}}\frac{\mathrm{d}}{\mathrm{d}\hat{s}}\boldsymbol{Q}\right) \tag{2}$$

where the ax operation returns the pseudovector associated with the skew-symmetric matrix $\boldsymbol{Q}^{\mathrm{T}}\mathrm{d}\boldsymbol{Q}/\mathrm{d}\hat{s}$. The ax operation acts on a skew symmetric matrix $\boldsymbol{S} = \begin{pmatrix} 0 & -c & b \\ c & 0 & -a \\ -b & a & 0 \end{pmatrix}$ such that $\mathrm{ax}(\boldsymbol{S}) = \boldsymbol{v} = (a,b,c)^{\mathrm{T}}$. Its inverse operation, skew, acts on $\boldsymbol{v}$ such that $\mathrm{skew}(\boldsymbol{v}) = \boldsymbol{S}$. These have the property that for any vector $\boldsymbol{x}$, $\boldsymbol{Sx} = \boldsymbol{v} \times \boldsymbol{x}$.

The components of $\boldsymbol{\kappa}$ along the reference triad vectors, $\kappa_\alpha = \boldsymbol{\kappa} \cdot \hat{\boldsymbol{d}}_\alpha$, measure the two bending strains, κ_1 and κ_2, and single
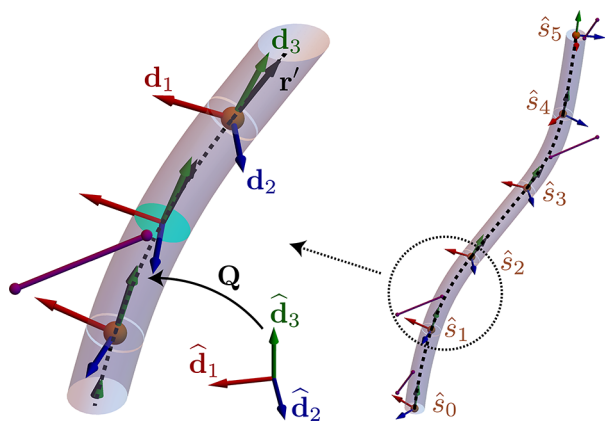
Figure 1. Quantities used to specify a thin rod's configuration in the Cosserat theory are illustrated. A deformed rod, to which surface linkers shown in purple are attached, has a backbone $r(\hat{s})$ shown as a black dashed curve, and a local triad of directors $d_\alpha(\hat{s})$ shown as red, blue, and green arrows. The matrix $D(\hat{s}) = (d_1(\hat{s}), d_2(\hat{s}), d_3(\hat{s}))$ is formed from these column vectors. The rotation tensor $Q(\hat{s})$ rotates the reference director triad $\hat{d}_\alpha$ to the current director triad $d_\alpha(\hat{s})$. In the Cosserat theory the local tangent of the backbone $dr/d\hat{s}$, shown as a black arrow, can differ from the local $d_3(\hat{s})$ director to allow for shear. The rod is discretized into segments which have end points defined by the knot-point coordinates $\hat{s}_i$, which are shown as orange spheres. In this visualization there are five segments and six knot points. The left panel displays a blow-up of the right panel, where the filament's cross-section is visualized as a cyan circle. Although the director triads are only visualized here at certain discrete positions along the filament, they can be found at any position given the continuous parametrizations used in the variational models.

twisting strain, κ_3, at each arc-length coordinate $\hat{s}$. Similarly, the components along $\hat{d}_\alpha$ of the vector

$$\sigma = Q^T \frac{dr}{d\hat{s}} - \frac{d\hat{r}}{d\hat{s}} \tag{3}$$

measure the two transverse shearing strains, σ_1 and σ_2, and the single stretching (extensional) strain, σ_3, completing the collection of six strain measures.

These strain components are used to define the elastic strain energy density $\varepsilon(\hat{s})$ of the rod's configuration in the Cosserat theory.[37,38] The filament's total strain energy E is obtained by integrating the density $\varepsilon(\hat{s})$ along the filament's reference arc-length $\hat{L}$:

$$E = \int_0^{\hat{L}} \varepsilon(\hat{s}) \, d\hat{s} \tag{4}$$

The most general quadratic expansion of the local energy density $\varepsilon(\hat{s})$ would include all 21 terms of the form $\kappa_\alpha \kappa_\beta$, $\kappa_\alpha \sigma_\beta$, and $\sigma_\alpha \sigma_\beta$, for $\alpha, \beta = 1, 2, 3$, capturing mechanical couplings between all components of the strain.[30,31] However, the material symmetries of the rod can significantly reduce the number of terms needed to describe the energy. An actin filament can be approximately classified as a transversely hemitropic (i.e., spatially averaged screw-symmetric) rod.[45] It can be shown that such a rod has an energy density with the form[37]

$$\varepsilon = \frac{S_{1,1}}{2}(\sigma_1^2 + \sigma_2^2) + \frac{B_{1,1}}{2}(\kappa_1^2 + \kappa_2^2) + \frac{S_{3,3}}{2}\sigma_3^2 + \frac{B_{3,3}}{2}\kappa_3^2$$
$$+ C_{1,1}(\sigma_1\kappa_1 + \kappa_2\sigma_2) + C_{3,3}\sigma_3\kappa_3 + C_{1,2}(\sigma_1\kappa_2 - \sigma_2\kappa_1) \tag{5}$$

The coefficients $S_{\alpha,\beta}$, $B_{\alpha,\beta}$, and $C_{\alpha,\beta}$ can be viewed as elements of the parameter matrices S, B, and C appearing in the general quadratic expression of ε.[38] They are geometric and material constants (rigidities) that parametrize the energy penalty of the rod in response to various deformations. The top row of terms in eq 5 captures the energy due to each mode of deformation individually. The bottom row, which would be zero for an isotropic material, captures couplings between these deformations. The twist-stretch coupling term proportional to $C_{3,3}$ is of particular interest in the case of actin, because it allows for chiral asymmetry in the filament's torsional compliance.[45,46] We note that other mechanical coupling terms not included in eq 5, such as a twist-bend coupling term proportional to $(\kappa_1 + \kappa_2)\kappa_3$, can also play a role in the mechanics of short actin filaments for which spatial averaging is a poor approximation.[30] Any such coupling terms, as well as higher order terms in the expansion of ε, could be easily accommodated by the methodology subsequently presented in this paper, but in our present applications we use eq 5 to describe chiral actin filaments.

To parametrize the model we need to specify the elements of S, B, and C which appear in eq 5. The diagonal elements of S and B can be expressed in terms of the material properties E_{mod} and G_{mod}, representing the Young's and shear moduli, respectively, and the geometric properties A, I, and α_c, representing the cross-sectional area, second (polar) moment of inertia tensor, and a constant equal to 4/3 for circular cross sections. We give the details of the parametrization in the Supporting Information, section 2.1. The elements of C will be treated here as tunable parameters to study the effect of anisotropic mechanical compliance. We note that the elements of C are bounded by the requirement of energy positivity; for instance $|C_{3,3}| < \sqrt{S_{3,3}B_{3,3}}$.[45]

2.2. Variational Approach to Rod Mechanics. In one standard modeling approach, the energy E is used to derive equations of motion which when numerically integrated propagate the rod's configuration forward in time.[36,41,47] Rather than numerically integrating a differential equation, which requires significant computational effort for large systems, the approach pursued in this paper is to efficiently find approximately equilibrated rod configurations under some external loads. In addition to the computational acceleration afforded by directly seeking minimized configurations, we are also motivated to pursue this approach because we aim to incorporate a filament model using the Cosserat theory into the simulation platform MEDYAN.[18] In MEDYAN, the system's dynamics are propagated forward via short bursts of stochastic chemical activity over a reaction-diffusion compartment grid followed by periodic relaxation of the system's mechanical energy; this allows for efficient simulations that include chemical reactions with spatially varying propensities.[48,49] We note that this energy-minimization based approach to dynamics neglects the thermal diffusive motion of the filaments. The rationale behind this approach is that the ATP-consuming contributions to the system dynamics, coming from myosin motor steps and actin polymerization, significantly outweighs the contributions coming from diffusive motion of the filaments in these far-from-equilibrium systems.[7,18,50] As a result, neglecting thermal motion in MEDYAN simulations is not expected to significantly compromise the realism of the behaviors in which we are interested, and this claim has been corroborated through

several validations of MEDYAN predictions against exper-imental measurements.[51−56] Under some external loads, such as cross-linkers bound to the filament, the energy E is variationally minimized for some continuous functions $r^{\star}(\hat{s})$ and $Q^{\star}(\hat{s})$, where the star denotes the energy-minimized configuration. This infinite-dimensional functional minimiza-tion problem is computationally burdensome, necessitating a more efficient scheme for scalable simulations.

The crucial approximation underlying our variational approach is similar in spirit to the Rayleigh-Ritz (or Ritz-Galerkin) method, in which an infinite-dimensional eigenvalue problem is converted to a finite-dimensional one via restriction to a finite-dimensional subspace of expansion coefficients for some chosen basis functions.[57,58] In our method, we assume that both $r(\hat{s})$ and $Q(\hat{s})$ are of a specified functional form having a discrete set of free parameters $\mathcal{K}$. We present two options for this: one in which $r(\hat{s})$ and the Euler angles parametrizing $Q(\hat{s})$ are spline functions of $\hat{s}$, and one in which $Q(\hat{s})$ is the geodesic curve in SO(3) (the three-dimensional rotation group) on a segment of the filament while $dr/d\hat{s}$ is parametrized using its components in the local $d_\alpha(\hat{s})$ basis. The details of these functional forms are elaborated below. The strain energy density $\varepsilon(\hat{s}; \mathcal{K})$ becomes a function of $\hat{s}$ and the parameters $\mathcal{K}$ through its definition in terms of the strain components, eq 5. The key challenge in this variational approach is evaluating the integral in eq 4 to express the total energy of the filament $E(\mathcal{K})$ as a function of the model parameters. Once this is done, equilibrated configurations of the rod under some external loads, whose energy $E_{\text{ext}}(\mathcal{K})$ is also expressed in terms of the model parameters, are found by minimizing the total energy $E_{\text{tot}}(\mathcal{K}) = E(\mathcal{K}) + E_{\text{ext}}(\mathcal{K})$ with respect to the elements in $\mathcal{K}$. This yields the optimized parameters $\mathcal{K}^{\star} = \arg\min_{\mathcal{K}} E_{\text{tot}}(\mathcal{K})$, which determine the optimized configuration $r^{\star}(\hat{s}) = r(\hat{s}; \mathcal{K}^{\star})$ and $Q^{\star}(\hat{s}) = Q(\hat{s}; \mathcal{K}^{\star})$. We find that, using the spline representation for $r(s; \mathcal{K})$ and the Euler angles of $Q(\hat{s}; \mathcal{K})$, it is necessary to expand $\varepsilon(\hat{s}; \mathcal{K})$ around small values of the Euler angles for the integral in eq 4 to be analytically solvable. Using the geodesic form for Q, this approximation does not need to be made. We next give the details of these two variational methods.

2.3. Spline-Based Models. Here we describe how to assign a functional form for the rod's configuration, $r(\hat{s})$ and $Q(\hat{s})$, using spline functions. We refer to this approach as the "spline-based" model. Commonly used in the field of computer graphics, several spline functions are available such as B-splines, exponential splines, and Hermite splines, which may each have particular advantages depending on the application.[59−62] For the purpose of demonstrating this approach, we use here composite Bézier curves which are fairly intuitive and easy to use, but this method could be straightforwardly extended to using other splines. The reference arc-length $\hat{L}$ is discretized into $N_k − 1$ segments whose ends are N_k knot coordinates. The knot coordinates are particular values $\hat{s}_i$ of the reference arc-length, and the ith segment has a reference arc-length $\hat{L}_i = \hat{s}_{i+1} − \hat{s}_i$. This discretization is illustrated in Figure 1.

A composite Bézier curve $x(\hat{s})$ is a piecewise function which passes through N_k knot points x_i, where $i = 0, ..., N_k − 1$. On each segment i, $x(\hat{s})$ is a polynomial of order d whose shape is controlled by the control points $x_{i,j}$, where $j = 0, ..., d − 2$ and

the double index indicates that $x_{i,j}$ is a control point. Like N_k, the polynomial order d is a hyperparameter controlling the complexity of the model. We will formulate the model for general values of these hyperparameters, but in our implementations we choose d as 1 or 2 and N_k such that an actin filament segment is ∼20−100 nm long. In Figure 1, for instance, we have $N_k = 6$ which is a typical value used. The full curve $x(\hat{s})$ consists of $N_k − 1$ segments $x_i(\hat{s})$, $i = 0, ..., N_k − 2$, such that $x(\hat{s}) = x_i(\hat{s})$ if $\hat{s}_i \leq \hat{s} < \hat{s}_{i+1}$. Here the argument of $x_i(\hat{s})$ indicates that it is a function rather than a knot point. The segment curves $x_i(\hat{s})$ are reparameterized using the segment variable $q(\hat{s}; \hat{s}_i, \hat{s}_{i+1}) = (\hat{s} − \hat{s}_i)/\hat{L}_i$ which ranges from 0 to 1 as $\hat{s}$ increases from $\hat{s}_i$ to $\hat{s}_{i+1}$. In terms of q, the segment curves are given by the formula

$$x_i(q) = (1 − q)^d x_i + q^d x_{i+1} + \sum_{i=0}^{d-2} B_{j+1}^d(q) x_{i,j} \tag{6}$$

where the Bernstein polynomials are

$$B_j^d(q) = \binom{d}{j} q^j (1 − q)^{d-j} \tag{7}$$

If all knot and control points are free, then unphysical cusps can result in the composite curve at the knot points. To address this, smoothness up to degree p can be enforced through derivative matching conditions

$$\lim_{\hat{s} \to \hat{s}_{i+1}^-} x_i^{(k)}(\hat{s}) = \lim_{\hat{s} \to \hat{s}_{i+1}^+} x_{i+1}^{(k)}(\hat{s}) \tag{8}$$

where $i = 0, ..., N_k − 3$, $k = 1, ..., p$ and $x_i^{(k)}(\hat{s})$ denotes the kth derivative with respect to $\hat{s}$ of $x_i(\hat{s})$. Choosing $p = d − 1$ gives $3(d − 1)(N_k − 2)$ equations in $3(N_k + (N_k − 1)(d − 1))$ parameters, leaving $3(N_k + d − 1)$ free. These free parameters can be taken to be the N_k knot points x_i and the control points on the first segments, $x_{0,j}$, $j = 0, ..., d − 2$. This choice of p provides the greatest amount of smoothness while also allowing the number of free parameters to grow with N_k. One deficit of this parametrization is that specifying a position on the ith segments requires using parameters from segments 0 to $i − 1$, since the control points on the ith segment are determined from the smoothness constraints involving these previous parameters. However, for reasonably small values of N_k, up to ∼10, this issue does not significantly impair model performance (we discuss the computational efficiency of these models in the Supporting Information, section 1.3).

A composite Bézier curve is used to represent both the backbone curve $r(\hat{s})$ as well as the curve $\alpha^{\text{Eu}}(\hat{s})$, containing the Euler angles parametrizing $Q(\hat{s})$, as a function of $\hat{s}$. The vector $\alpha^{\text{Eu}}(\hat{s}) = (\phi^{\text{Eu}}(\hat{s}), \theta^{\text{Eu}}(\hat{s}), \psi^{\text{Eu}}(\hat{s}))^{\text{T}}$ encodes here the 3−2−1 (yaw-pitch-roll) Euler angles of Q, although other Euler angle conventions could also be used.[63] For this representation of $r(\hat{s})$ and $Q(\hat{s})$, the model parameters are

$$\mathcal{K} = \{r_{0,0}, ..., r_{0,d_r-2}, r_0, ..., r_{N_k-1}, \alpha_{0,0}^{\text{Eu}}, ..., \alpha_{0,d_\alpha-2}^{\text{Eu}}, \alpha_0^{\text{Eu}},$$
$$..., \alpha_{N_k-1}^{\text{Eu}}\}$$

where d_r and d_α are the orders of the composite Bézier curves for the backbone and Euler angles, respectively. Using the above definitions of the strain components which enter into eq 5, it is straightforward to write the strain energy density $\varepsilon(\hat{s}; \mathcal{K})$ using these spline parameters. However, to find the integrated energy $E(\mathcal{K})$, it is necessary due to the intractability

of analytically integrating $\varepsilon(\hat{s}; \mathcal{K})$ to make a small-angle approximation to $Q(\alpha^{\text{Eu}}) \approx Q_{\text{approx}}(\alpha^{\text{Eu}}; m)$. The order m of the small-angle expansion is an additional hyperparameter of the model. Using Q_{approx} in place of Q in the definition of the strain components, the approximate strain energy density $\varepsilon_{\text{approx}}(\hat{s}; \mathcal{K})$ becomes a polynomial in $\hat{s}$; that is

$$\varepsilon_{\text{approx}}(\hat{s}; \mathcal{K}) = \sum_k \varepsilon_k(\mathcal{K})\hat{s}^k \tag{9}$$

which may therefore be easily integrated to give the approximate energy of the filament $E_{\text{approx}}(\mathcal{K})$. We implemented a routine to calculate $E_{\text{approx}}(\mathcal{K})$ using the computer algebra system Mathematica.[64] The details of this calculation are tedious (though straightforward) and do not provide additional insight, so we do not present them here.

2.4. Geodesic Models. As discussed in section 3, the small-angle approximation used to obtain an analytical expression for the integral of the energy density in the spline-based model can lead to biased filament configurations that are highly inaccurate when the deformations are large. To address this issue, we next present a so-called "geodesic" model which avoids making the small-angle approximation and produces approximately correct filament configurations even for large deformations.

In the geodesic model, we adopt the axis-angle parametrization for the rotation tensor Q, rather than the Euler angle parametrization used above. In the axis-angle parametrization $Q(u, \theta)$ represents a rotation about the unit vector u by the angle θ. The Rodrigues formula expresses the tensor in terms of u and θ as

$$Q(u, \theta) = \cos(\theta)(E - u \otimes u) + \sin(\theta) \, \text{skew}(u)$$
$$+ \, u \otimes u \tag{10}$$

where E is the 3×3 identity matrix, the skew operation returns the skew-symmetric matrix associated with the unit vector u (and is the inverse of the ax operation), and $\otimes$ denotes the outer (dyadic) product.[38] $Q(u, \theta)$ can also be represented using matrix exponentiation as

$$Q(u, \theta) = \exp(\text{skew}(\theta u)) \tag{11}$$

This representation makes evident the connection between the orthogonal tensor Q, a member of the Lie group $SO(3)$, and the skew-symmetric tensor $\text{skew}(\theta u)$, a member of the associated Lie algebra $\mathfrak{so}(3)$.[65] The transpose $Q^T(u, \theta)$ can be obtained as $Q^T(u, \theta) = Q(u, -\theta)$.

We again use N_k knot coordinates to discretize the filament into $N_k - 1$ segments. At every knot coordinate $\hat{s}_i$ a rotation tensor Q_i is parametrized with free model parameters u_i^{Ax} and θ_i^{Ax}. To enforce normalization, we represent u_i^{Ax} in polar coordinates using the polar and azimuthal angles, β_i^{Ax} and γ_i^{Ax}, respectively. Thus, the collection of angles θ_i^{Ax}, β_i^{Ax}, and γ_i^{Ax} parametrize Q_i at $\hat{s}_i$. On the ith segment (where $\hat{s}_i \leq \hat{s} < \hat{s}_{i+1}$), the rotation tensor $Q_i(q)$ is taken to be the geodesic curve on the manifold $SO(3)$ which connects the two tensors Q_i and Q_{i+1}, where $q(\hat{s}; \hat{s}_i, \hat{s}_{i+1}) = (\hat{s} - \hat{s}_i)/\hat{L}_i$ is the local segment variable as in the spline-based model. The geodesic curve depends on the metric D used to define distances in $SO(3)$, and we use the metric

$$D(Q_A, Q_B) = |\theta_{A,B}| \tag{12}$$

where $\theta_{A,B}$ is the angle in the axis-angle parametrization of the tensor $Q_B Q_A^T$ rotating Q_A to Q_B.[66] It can be shown that the geodesic curve $Q_i(q)$ connecting Q_i and Q_{i+1} using this metric is

$$Q_i(q) = \exp(q \ln(Q_{i+1} Q_i^T)) Q_i \tag{13}$$

where ln is the matrix logarithm.[67,68] As described in the Supporting Information, section 2.2 this curve can then be expressed in terms of the free model parameters θ_i^{Ax}, β_i^{Ax}, γ_i^{Ax}, θ_{i+1}^{Ax}, β_{i+1}^{Ax}, and γ_{i+1}^{Ax}. The global tensor curve $Q(\hat{s})$ is given piecewise by $Q_i(\hat{s})$ on the $N_k - 1$ segments.

To represent the backbone curve $r(\hat{s})$ in the geodesic model, we write its derivative with respect to $\hat{s}$ in the local director triad basis d_α:

$$\frac{dr(\hat{s})}{d\hat{s}} = \zeta_\alpha(\hat{s}) d_\alpha(\hat{s}) \tag{14}$$

where summation over repeated indices is implied. Here we treat the components $\zeta_\alpha(\hat{s})$ as constants on each segment, i.e. $\zeta_\alpha(\hat{s}) = \zeta_{i,\alpha}$ for $\hat{s}_i \leq \hat{s} < \hat{s}_{i+1}$, although this assumption could be relaxed. The piecewise constant components $\zeta_{i,\alpha}$ are additional free model parameters. We refer to the model where $\zeta_{i,\alpha}$ are all independent as the "geodesic Cosserat" (GC) model. We can also optionally set $\zeta_{i,1} = \zeta_{i,2} = 0$ on all segments, implying that $dr/d\hat{s}$ is everywhere parallel to $d_3(\hat{s})$ such that there is zero shear on the filament. The filament is still extensible, since $\zeta_{i,3} \neq 0$, so this model is referred to as the "geodesic extensible Kirchoff" (GEK) model. To obtain the backbone curve $r(\hat{s})$, we integrate $dr/d\hat{s}$ from the minus-end position of the filament $r_0 = r(\hat{s} = 0)$, as shown in the Supporting Information, section 2.2. The initial point r_0 is the final free parameter in the GC and GEK models. We note that the filament energy $E(\mathcal{K})$ will not depend on r_0 due to translation invariance, but external potentials $E_{\text{ext}}(\mathcal{K})$ such as cross-linkers bound to the filament will depend on r_0. For the GC model, there are $6N_k$ elements in $\mathcal{K}$, while for the GEK model there $4N_k + 2$.

A significant benefit of the geodesic parametrization of $r(\hat{s})$ and $Q(\hat{s})$ is that it allows the energy density to be analytically integrated along the length of the filament to give an exact expression for the total filament energy $E(\mathcal{K})$. We describe the derivation of this expression in the Supporting Information, section 2.3. As an intuitive picture, the geodesic curves used in this model can be thought of as representing a "linear" interpolation between rotation tensors in their natural mathematical space, and they are therefore expected to be a useful tool for parametrizing how several free rotation tensors are connected together.

2.5. MEDYAN Model. For comparison, we describe here the original zero-width mechanical model used in the simulation platform MEDYAN.[18] This model has no allowed shearing or twisting, although excluded volume repulsion is included between filaments using a finite effective filament radius.[19] The energy in this model does allow for stretching and bending. The filament is again discretized into N_k knot coordinates and $N_k - 1$ segments. Each segment is a straight line with a current length $L_i = s_{i+1} - s_i$ and a reference length $\hat{L}_i = \hat{s}_{i+1} - \hat{s}_i$. The stretching energy on each segment is a quadratic function of these lengths:

$$E_i^{\text{stretch}} = \frac{S_{3,3}}{2\hat{L}_i}(L_i - \hat{L}_i)^2 \tag{15}$$

The segment acts like a spring with spring constant $S_{3,3}/\hat{L}_i$. At each internal knot coordinate there is a bending potential involving the angle $\theta_{i,i+1}^{MED}$ between the ith and $(i + 1)$th segment:

$$E_i^{bend} = \frac{B_{1,1}}{\hat{L}_i}\left(1 - \cos\left(\theta_{i,i+1}^{MED}\right)\right) \qquad (16)$$

where $i = 1, ..., N_k - 2$. We show in the Supporting Information, section 2.3 that this expression for the bending energy can be obtained as a special case of the GC model bending energy. In the MEDYAN model, the knot points r_i are the only free parameters, and the backbone curve $r(\hat{s})$ is a linear interpolation between these points. There are thus $3N_k$ elements in $\mathcal{K}$ for this model.

2.6. Dynamical Model. We also briefly describe for comparison the dynamical model of a filament developed by Gazzola et al. in ref 36. Rather than directly seeking equilibrated configurations of the filament, the dynamical approach propagates the filament's configuration forward in time using discretized equations of motion based on the forces and torques in the filament. Propagating the configuration forward for long times with dissipation will cause the filament to converge to its equilibrated configuration under some external loads. The filament in this model is discretized into $N_n - 1$ linear segments which, when N_n is large, allows for a good approximation to any arbitrary filament backbone configuration. In our use here, we take $N_n \gg N_k$, so there are far fewer degrees of freedom in the variational models than in the dynamical model. The backbone $r_i(t)$ is specified at each of the N_n coordinates, and the rotation tensor $Q_i(t)$ is specified on each of the $N_n - 1$ segments. These quantities are updated in discrete time steps δt using a second-order velocity Verlet integrator scheme. The equations of motion correspond to an isotropic energy function given by the top row of terms in eq 5. For fine spatial and temporal discretization this model has been shown to be very expressive, capturing a range of realistic filament behaviors, and we use it in this paper as the "ground truth" to which our computationally accelerated variational models can be compared to assess their accuracy. We refer the reader to ref 36 for details of this model, and to the follow-up paper, ref 1, in which extensions to this dynamical model are developed to treat multiple spatial scales simultaneously.

2.7. Binding to Surface. In one-dimensional filament models like the original MEDYAN model, external loads such as bound cross-linkers on the filament are attached directly to the filament backbone. In the new models presented above, the filament has a finite width, and external loads may attach to the surface of the filament, exerting shearing and twisting forces. This introduces an extra degree of freedom at the attached arc-length coordinate $\hat{s}^b$ corresponding to the position on the perimeter of the filament's cross-section at $\hat{s}^b$ to which the load is attached. This cross-section is spanned by the vectors $d_1(\hat{s}^b)$ and $d_2(\hat{s}^b)$, and the one-dimensional position on the perimeter of the cross-section can be parametrized by the polar angle ϕ^b with respect to the local $d_1(\hat{s}^b)$ axis. For a circular cross section, the position of the attached load is given by

$$r^b = r(\hat{s}^b) + R(\cos(\phi^b)d_1(\hat{s}^b) + \sin(\phi^b)d_2(\hat{s}^b)) \qquad (17)$$

where R is the filament radius. This position therefore couples not just to the backbone $r(\hat{s}^b)$ but also to the local rotation tensor $Q(\hat{s}^b)$ through $d_\alpha(\hat{s}) = Q(\hat{s})\hat{d}_\alpha$. This binding of an attached linker to the local perimeter of the filament cross-section is illustrated in Figure 2.
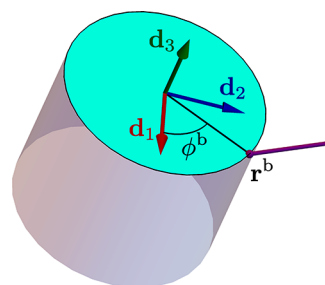
Figure 2. Cross-section of a filament with a bound cross-linker is shown. The cross-linker is visualized in purple and the local director triad is visualized as a set of colored vectors. The angle ϕ^b and bound position r^b appearing in eq 17 are also illustrated.

In simulation packages like MEDYAN, filament binding reactions occur stochastically according to local chemical propensities. During a simulated binding event, the angle φ^b could be chosen in several ways, which we describe in the Supporting Information, section 2.4. For example, to provide additional biological realism one could fix ϕ^b for the possible binding sites to lie along a helix which wraps around the filament. In this way, the helical microstructure of actin could be encoded into the available binding sites.

3. RESULTS

Here we present both validation and application results using the models described above. Model validation is done by comparing the equilibrated filament configurations for different test cases to the finely discretized dynamical model of Gazzola et al., which we take to be the ground truth.[36] The results indicate that under small applied loads all models agree well, but for larger applied loads the geodesic models, which avoid the small-angle approximation, perform significantly better than the spline-based models which exhibit systematic bias. In the Supporting Information, section 1.1, we show that the geodesic models also better reproduce the theoretical predictions of Euler buckling compared to the spline-based models. The original zero-width MEDYAN model also produces systematically unbiased rod configurations under large deformations but does not allow for finite filament widths. Next, to demonstrate a novel application of the new finite-width models, we simulate a "chiral bundle," a group of seven filaments with nonzero chiral coupling rigidity $C_{3,3}$ interconnected by surface-bound cross-linkers. Pulling vertically on the bundle induces a twist of each filament which, through the attached cross-linkers, causes the entire bundle structure to adopt a twisted configuration. Such a structure may be relevant to the physiological functioning of actin stress fibers in eukaryotic cells and also demonstrates the possibility of intrinsic filament chirality propagating up a spatial scale to break chiral symmetry in the structure of a cross-linked bundle.[69] Finally, we demonstrate the feasibility of using the geodesic model to study network-level cytoskeletal dynamics by implementing it into MEDYAN.

3.1. Model Comparisons. To assess the accuracy of the spline-based and geodesic models introduced above, we compare their equilibrated configurations to the steady state configuration of the finely discretized dynamical model with

dissipation. Five models are compared against the dynamical model: the Bézier spline-based model with a first order small-angle expansion ("B, $m = 1$"), the Bézier spline-based model with a second order small-angle expansion ("B, $m = 2$"), the geodesic extensible Kirchoff model (GEK), the geodesic Cosserat model (GC), and the original MEDYAN model. To quantify the difference between the equilibrated configurations, we use two similarity measures. The first, C_r, measures the root-mean-squared distance between the backbone curves of two filaments A and B:

$$C_r(\boldsymbol{r}^A(\hat{s}), \boldsymbol{r}^B(\hat{s})) = \left(\hat{L}^{-1} \int_0^{\hat{L}} \| \boldsymbol{r}^A(\hat{s}) - \boldsymbol{r}^B(\hat{s}) \|^2 \, \mathrm{d}\hat{s} \right)^{1/2} \tag{18}$$

where $\|\cdot\|$ denotes the vector norm. The second similarity measure, C_d, is introduced to measure the average difference in the vectors $\boldsymbol{d}_3^A(\hat{s})$ and $\boldsymbol{d}_3^B(\hat{s})$ along the reference arc-length:

$$C_d(\boldsymbol{d}_3^A(\hat{s}), \boldsymbol{d}_3^B(\hat{s})) = \hat{L}^{-1} \int_0^{\hat{L}} (1 - \boldsymbol{d}_3^A(\hat{s}) \cdot \boldsymbol{d}_3^B(\hat{s})) \, \mathrm{d}\hat{s} \tag{19}$$

Both C_r and C_d are evaluated numerically using a large number of sample points.

Three test cases, labeled (A), (B), and (C) in Figure 3 were used to assess the models' accuracy. The deformation in each test case is in a 2D plane so that the configurations can be easily visualized. In test case (A), a 500 nm-long filament is pulled by four springs in opposing directions, while in test cases (B) and (C), a 100 nm long filament is pulled by three springs. Test cases (B) and (C) are distinguished by the strength of the pulling such that the springs in test case (C) are much more stretched than those in (B), causing a greater filament deformation. The filaments in each test case are modeled as isotropic (with the coupling matrix elements $C_{\alpha,\beta}$ in eq 5 set to zero), and the springs attach directly to the filament backbone. This is done to allow comparison with the original MEDYAN model and the dynamical model implementations, which do not currently support anisotropic filaments or surface-bound cross-linkers. The details of the set up for these test cases are described in the Supporting Information, section 1.2.

For the three test cases, we generally observed that the closest agreement with the dynamical solution was obtained by the geodesic models; however, for the small deformations in test case (B) all models agree well with each other (see Table 1). This indicates the sufficiency of the small-angle approximation for small applied loads. For large loads, the spline-based models have systematically smaller deformations than the geodesic and dynamical models, which is a major shortcoming. The original MEDYAN model does not exhibit this systematic error, though it is less precise due to its linear segment shapes. The difference between the GEK and GC models is negligible for all test cases, resulting from the high shearing modulus of actin; the extra degrees of freedom in the GC model should still be useful for modeling other types of filaments. Both geodesic models agree very well with the dynamical solution, with only slight differences in shape even for large applied loads. Minimizing the geodesic models to obtain the equilibrated configurations takes on the order of seconds of computational time; however, whereas propagating the finely discretized dynamical model until it is equilibrated takes on the order of days. We display in the Supporting Information, section 1.4 the profile of shearing, extensional,
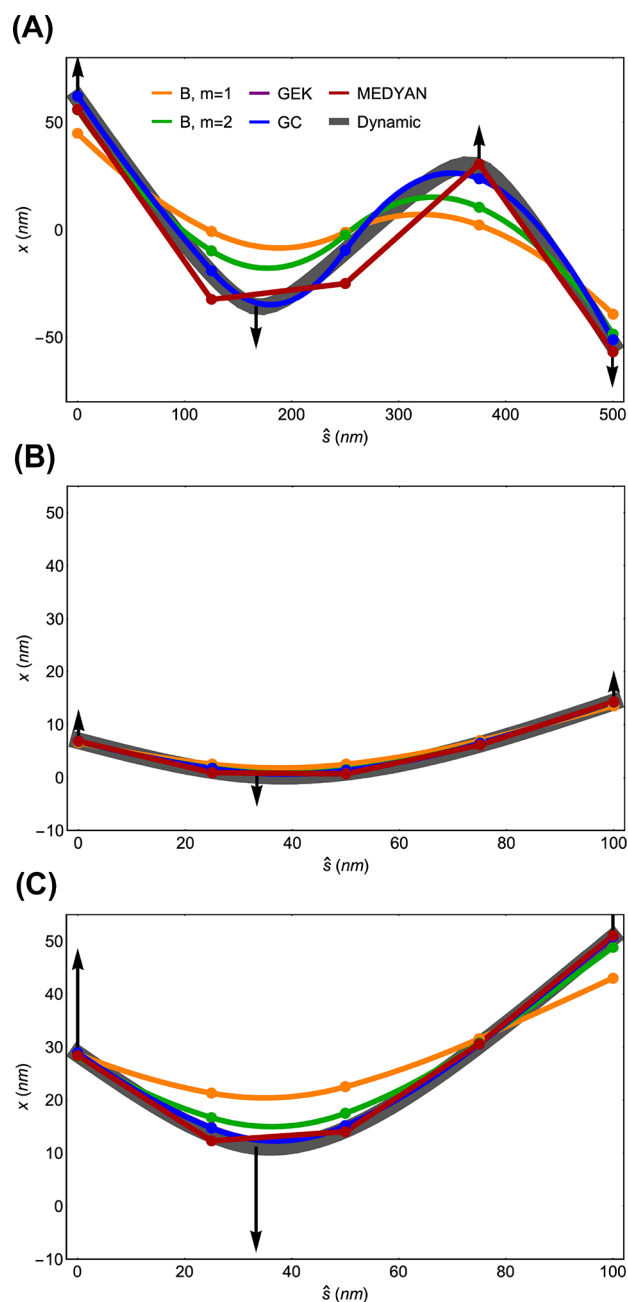
Figure 3. A comparison of the variational and dynamical models is shown. (A) The equilibrated backbone curve, projected onto the x-axis, for the five variational models and the dynamical model is shown in the bottom plot, colored according to the legend. This panel corresponds to the first test case described in the main text. The five knot points of the variational models are shown as solid circles through which the curves pass. The black arrows attached to the dynamical solution's curve indicate the attachment point and direction of the bound cross-linkers, and the arrow lengths are proportional to the x coordinate of the cross-linkers' other ends. (B) (respectively (C)) This panel is the same as panel (A), except it applies to the second (respectively third) test case described in the main text. We note that the GEK model curve is closely matched by the GC model curve and is hidden behind it in these graphs.

bending, and twisting strain for the variational models along the length of the equilibrated filament for the third test case. We also show in the Supporting Information, section 1.3 the computational timing of the variational models along with their

Table 1. Difference Metrics C_r and C_d between Each Model and the Dynamical Model for the Three Test Cases in Figure 3

s	metric	B, m = 1	B, m = 2	GEK	GC	MEDYAN
(A)	C_r (nm)	18.40	13.05	3.89	3.86	9.16
	C_d	0.041	0.022	0.008	0.008	none
(B)	C_r (nm)	1.06	0.39	0.30	0.28	0.23
	C_d	0.001	0.000	0.000	0.000	none
(C)	C_r (nm)	6.31	2.69	0.84	0.80	0.93
	C_d	0.036	0.011	0.000	0.001	none

accuracy as N_k is varied. Finally, we show in Table 2 the equilibrated filament and spring energies for each test case. We see that in each case the dynamical model achieves the smallest total energy of all models, which we might expect due to its comparative lack of restrictions on the filament configuration. However, the agreement in energy between the geodesic models and the dynamical model is excellent. Although in these test cases the difference between the GEK and GC models is small, we expect that in the context of real cytoskeletal networks, where molecular motors and branching molecules bind to the surfaces of filaments, the shearing degrees of freedom in the GC will be important. Such bound molecules can produce localized shearing forces which would not be resolved in the GEK model.

3.2. Bundle Study. Here we apply the new variational models to explore the induced chirality of a bundle of cross-linked actin filaments. The intuition underlying this study is based on actin stress fibers, which are bundles comprising ~7−20 filaments under significant tensile stress that transmit cell-wide forces during processes like cell migration.[2,51] The chiral coupling between axial stretching and filament twisting, captured by the $C_{3,3}$ parameter, opens the possibility that the filaments in a stress fiber also experience significant torsion under axial stress. We hypothesize that, due to the finite width of the actin filaments, this torsion will move the attached point of the bound cross-linker protein which will in turn pull on the other filaments to which it is bound. This will cause the peripheral filaments to tilt with respect to the central filament, such that the entire bundle structure acquires a helical pitch due to the applied tension, the twist-stretch coupling, and the bound cross-linkers.

To explore this possible effect, we simulated seven filaments, each 500 nm long and 7 nm in diameter, in a bundle connected

by three sets of cross-linkers attached in a spoke and rim pattern, as visualized in Figure 4A,B,C. Each filament
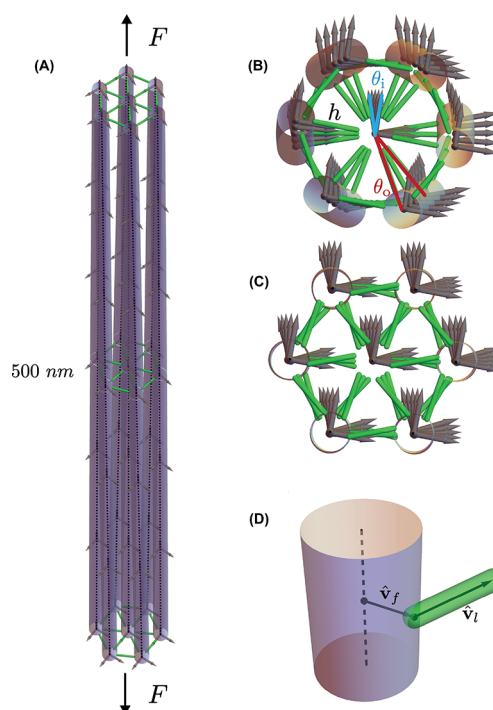

Figure 4. Structural details of the chiral bundle simulation are shown. (A) A side-on view is shown of a bundle of seven filaments. Each filament is 500 nm long, lies along the z-axis, and has 3 sets of cross-linkers (shown in green) attached at its ends and midpoints to each of its neighboring filaments. A constant force F is applied to each filament at both ends, causing each filament to undergo a twist due to the twist-stretch coupling when $C_{3,3} \neq 0$ pN nm. (B) A top-down view of the same bundle is shown, illustrating more clearly the rotation of the outer filaments around the central filament. The resting length of the cross-linkers is h. Red and blue wedges are drawn to illustrate the outer and inner angles θ_o and θ_i describing the bundle's twist. It is shown how the steric penalty ($\varepsilon_{\text{steric}} \neq 0$) can cause $|\theta_i| \approx |\theta_o|$. (C) Without the steric penalty, the filaments tend to move inward rather than tilt and bend around the central filament, such that $|\theta_i| > |\theta_o| \approx 0$. (D) An illustration is shown of the unit vectors $\hat{v}_f$ and $\hat{v}_l$ used in the definition of the steric interaction energy, eq 21.

represented using the B, m = 1 model with three knot points. Despite its less accurate performance under large applied loads (as shown in Figure 3), this model was observed to be

Table 2. Equilibrated Filament Energies E, External Energies from Bound Linkers E_{ext}, and Total Energy E_{tot} for the Three Test Cases in Figure 3 (All Units pN nm)

case	energy	B, m = 1	B, m = 2	GEK	GC	MEDYAN	dynamic
(A)	E	6 458	10 179	6 351	6 365	3 986	6 806
	E_{ext}	104 842	81 320	66 038	65 978	65 531	60 024
	E_{tot}	111 300	91 499	72 389	72 343	69 517	66 830
(B)	E	712	900	936	940	935	980
	E_{ext}	4 423	4 115	4 068	4 056	4 065	3 961
	E_{tot}	5 135	5 015	5 004	4 996	5 000	4 941
(C)	E	3 895	6 966	8 689	8 689	8 160	9 099
	E_{ext}	95 747	87 669	84 076	83 990	84 792	82 989
	E_{tot}	99 642	94 635	92 765	92 679	92 952	92 088
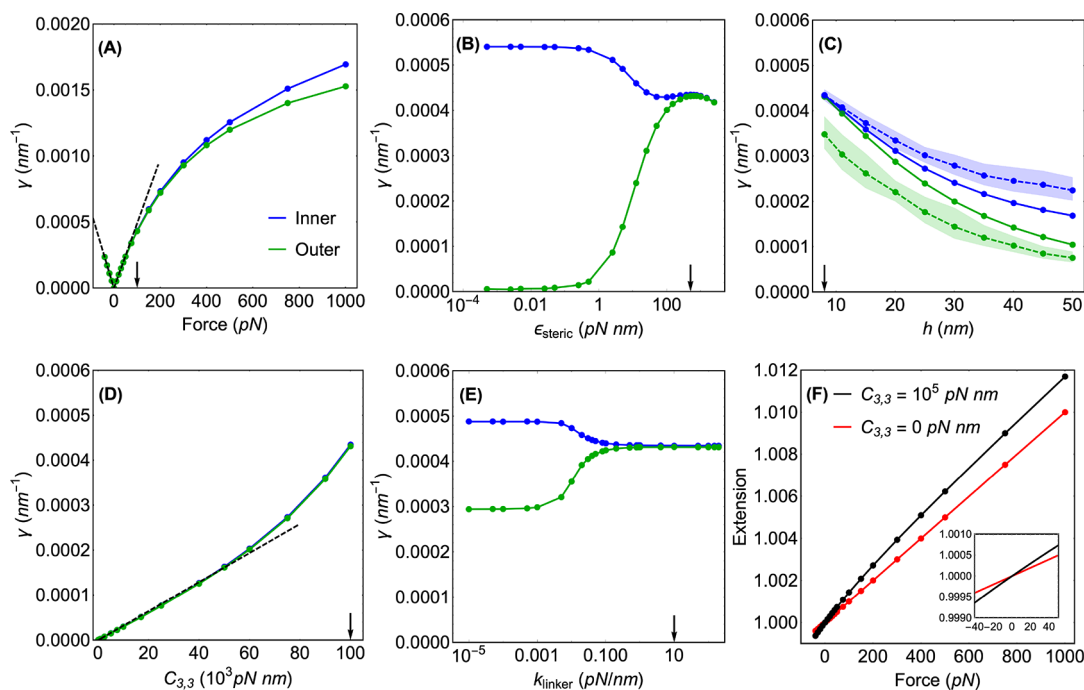
Figure 5. Results from the chiral bundle simulation are shown. (A) Plot of the inner (blue) and outer (green) rotation magnitude per unit length, measured in radians per nanometer, as the force F is varied. The black arrow indicates the value of F used when the other parameters are varied, and similarly for the arrows in the other plots. The black dashed lines show the linear response around $F = 0$ pN. (B) Plot of the inner and outer γ as $\varepsilon_{\text{steric}}$ is varied. (C) Plot of the inner and outer γ as h is varied. The dashed line and shaded area indicate the mean and standard deviation of 100 realizations of randomly placing three cross-liners between the pairs of filaments, rather than attaching them at the ends and filament midpoint. (D) Plot of the inner and outer γ as $C_{3,3}$ is varied. (E) Plot of the inner and outer γ as k_{linker} is varied. (F) Plot of the relative extension $L/\hat{L}$ as F is varied for two values of the coupling parameter $C_{3,3}$. The inset is a blow-up around $F = 0$ pN showing the crossover behavior.

consistent with other models tested for this study, and we use it here because it produced the cleanest trends due to its easily minimized energy function. The axial tension of a stress fiber was modeled by applying a constant z-direction force F in opposite directions to both ends of every filament in the bundle. The attached cross-linkers have a stretching energy given by

$$E_{\text{linker}} = \frac{k_{\text{linker}}}{2}(l - h)^2 \qquad (20)$$

where l is the cross-linker's instantaneous length and h is its rest length. With only this energy included, the peripheral filaments in the bundle tend to twist under tension and move inward toward the bundle center, allowing the lengths of the cross-linkers to achieve their rest lengths without causing the filaments to tilt (see Figure 4C). Certain actin binding proteins such as Arp2/3 are known to form relatively rigid angles with respect to the actin filament.[70] To account for this possibility, we also include a steric interaction which penalizes cross-linker orientations deviating from the local surface normal of the filament, with an energy given by

$$E_{\text{steric}} = \varepsilon_{\text{steric}}(1 - \hat{\boldsymbol{v}}_f \cdot \hat{\boldsymbol{v}}_l) \qquad (21)$$

where the unit vector $\hat{\boldsymbol{v}}_f$ denotes the local surface normal and $\hat{\boldsymbol{v}}_l$ denotes the unit vector pointing along the cross-linker's length from the local attachment point (see Figure 4D for an illustration of these vectors). This steric geometric penalty has the effect that the bundle is less compressible, such that filaments are less able to move toward the bundle center and will instead tend to tilt and rotate to satisfy the linker length penalty. The adjustable parameters of this setup are F, $C_{3,3}$,

$\varepsilon_{\text{steric}}$, k_{linker}, and h. We independently varied these parameters one at a time, holding the other parameters at their default values of $F = 100$ pN, $C_{3,3} = 10^5$ pN nm, $\varepsilon_{\text{steric}} = 500$ pN nm, $k_{\text{linker}} = 10$ pN/nm, and $h = 8$ nm.

We distinguish between the inner and the outer rotation of the bundle under tension. The inner rotation θ_i is the angle through which the central filament is twisted from its minus end to its plus end, and we define $\gamma_i = |\theta_i|/\hat{L}$ as the rotation per unit length. To measure the tilting of the peripheral filaments around the central filament, we define the outer rotation θ_o as a function of the distance δr by which a given outer filament's end points are separated from each other when projected to the xy-plane. If the distance from a peripheral filament's end point to the central filament's end point (i.e., the radius of the bundle) is a, then the outer rotation angle is defined as $\theta_o = \arccos(1 - (\delta r)^2/2a^2)$, given per unit length as $\gamma_o = |\theta_o|/\hat{L}$ (see Figure 4B for an illustration of these angles). The inner rotation $|\theta_i|$ will always be greater than or equal to $|\theta_o|$, and if the cross-linkers perfectly transmit the rotation of the filaments into the tilting of the outer ring, then $|\theta_i| = |\theta_o|$.

Several notable trends are observed in this study, displayed in Figure 5. First, we find a transition from a linear dependence of both γ_o and γ_i on F to sublinear dependence, at which point the outer and inner rotations also begin to separate from each other so that $\gamma_i > \gamma_o$ (Figure 5A). This behavior is also symmetric about $F = 0$, with compression inducing twisting in an approximately equal but opposite amount to stretching for small loads. These observations qualitatively agree with the intuition of linear response for small disturbances transitioning to nonlinear response for large disturbances. We also find a
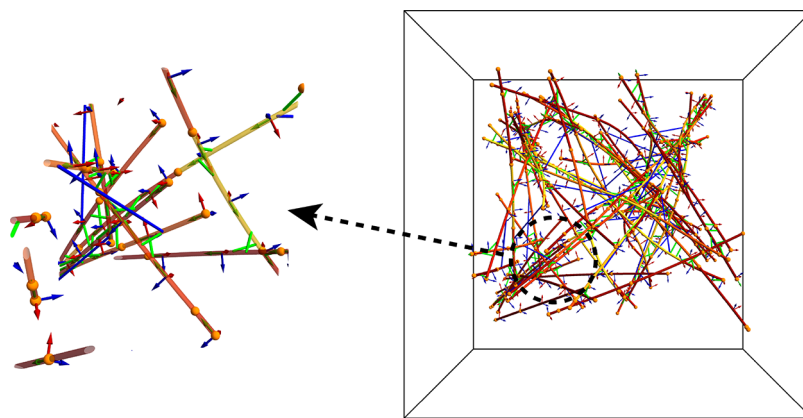
Figure 6. A visualization of a contractile actomyosin network from a MEDYAN simulation is shown, in which actin filaments are drawn as red-orange-yellow tubes, myosin minifilaments are shown as blue cylinders, and α-actinin cross-linkers are shown as green cylinders. The color of the actin filament segments ranges from red to yellow in proportion to the magnitude of the local twisting strain $|\kappa_3|$. The left panel shows a blow-up of a region of the full network in which additional detail of the surface-bound minifilaments and cross-linkers can be seen. The director triads, which are defined at every point on the actin filaments, are visualized as periodically spaced red, green, and blue arrows. The orange spheres represent the knot coordinate points, and the black box represents the simulation boundary. The snapshot is taken after 150 s of simulated time.

transition from linear to superlinear dependence on $C_{3,3}$ (Figure 5D).

Second, we find a strong nonlinear dependence of γ_o and γ_i on ε_{steric} reminiscent of a second-order phase transition (Figure 5B).[71] Below an apparent threshold around $\varepsilon_{steric} \approx$ 0.1 pN nm the applied force rotates the central filament by a fixed amount and the peripheral filaments rotate and move inward to satisfy the cross-linker length energy penalty. Above this threshold, and in a continuous manner, the steric penalty causes the filaments to tilt and bend rather than move inward to satisfy the cross-linker length penalty, causing γ_o to increase and γ_i to decrease. Above an upper threshold around $\varepsilon_{steric} \approx$ 100 pN nm this trend saturates, and only small, though interestingly nonmonotonic, changes are observed in γ_i and γ_o which now roughly coincide. Similar behavior is found for the dependence on k_{linker}, although the outer rotation below the lower transition threshold ~0.01 pN/nm is constant at a finite value, not zero, implying that the steric penalty alone can cause outer rotation of the bundle (Figure 5E).

Third, we find that as the cross-linker resting length h is increased, both γ_i and γ_o monotonically decrease, and γ_i grows relative to γ_o suggesting less effective transduction of inner rotation to outer rotation for large linker lengths (Figure 5C). We also tested the effect of randomly placing the cross-linkers between the filaments rather than at the ends and midpoint of the filaments, controlling for the number of cross-linkers between each pair. For each value of h, we sampled 100 realizations of cross-linker positions with uniform probability along the filament lengths. We expected that the ordered (but statistically unlikely) arrangement of cross-linkers enhances the transduction of inner to outer rotation because the forces throughout the bundle are highly coordinated. The rare configuration with ordered cross-linkers is indeed more effective at causing outer rotation than the typical random configuration, as shown by the dotted lines in Figure 5C which have larger γ_i and smaller γ_o for all h.

Finally, we tested how the mechanical coupling between twisting and stretching affected the force−extension curve of the bundle, shown in Figure 5.F. The equilibrated length L of the central filament was measured as a function of the pulling force and divided by its initial value $\hat{L} = 500$ nm to give the

relative extension. We found that a nonzero $C_{3,3}$ allows for greater extension and greater compression for a given force F. For $C_{3,3} = 0$ pN nm the force−extension curve is perfectly linear, while for $C_{3,3} \neq 0$ pN nm it smoothly interpolates between an asymptotically linear regime for $F \gg 0$ pN and a nonlinear crossing regime around the point $C_{3,3} = 0$ pN nm, $F = 0$ pN.

3.3. MEDYAN Implementation. As a final application, we implemented the GC model into MEDYAN.[18] This implementation consists of several new modeling choices, which we describe in detail in the Supporting Information, section 2.4. These new modeling choices have to do with allowing for chemical reactions, such as cross-linkers and molecular motors binding to filaments and filament polymerization and depolymerization reactions, using the new filament mechanical model presented in this paper. These additional chemical considerations, which allow the current mechanical model to be incorporated in a versatile active matter simulation platform, should significantly expand the model's usefulness in studying cytoskeletal dynamics.

In Figure 6 we show a snapshot from a MEDYAN simulation, in which an actomyosin network comprising physiological concentrations of actin, myosin (nonmuscle myosin IIA), and cross-linkers (α-actinin) has undergone a network-wide contraction away from the simulation boundaries. This motor-driven contraction is in keeping with well-documented behavior of actomyosin networks at these concentrations.[11,18,72] The key point is that the network in Figure 6 has binding molecules attached to the surfaces of the actin filaments rather than their backbones, allowing for network-level shearing and twisting forces, filament rotational dynamics, and chiral phenomenon to be studied *in silico*. The filament segments are colored according the local twisting strain κ_3, illustrating that torsional mechanics can now be modeled in self-organizing networks. We report here only the feasibility of implementing the GC model into a network-level simulation platform like MEDYAN, rather than any trends observed using this implementation which we plan to explore in future works.

4. DISCUSSION

An important physical feature currently missing from large-scale mechanochemical simulations of cytoskeletal networks is the finite width of the filaments. This precludes studying effects in which filaments can rotate or shear in response to forces in the network, arising for instance from bound molecular motors or polymerization against a boundary. To address this, we have presented in this paper a set of options for parametrizing the configurations of filaments with finite widths in a computationally efficient way, requiring only a small number of free model parameters. We focused here on variational models, in which we explore functional forms for a filament's mechanical degrees of freedom in order to efficiently find their equilibrated configurations. We introduced two main classes of functional forms: one in which a sequence of splines is used to parametrize the filament configuration, and one in which a sequence of geodesic curves in the space of orthogonal rotation tensors is used. In the spline-based approach, the intractable expressions for the strain components necessitated a small-angle expansion of the energy function. This was not necessary in the geodesic approach due to simplifications in the expressions of the strain components arising from the geodesic curve parametrization. This small-angle approximation is commonly made in treatments of elastic rods, but is shown here to give rise to significant deviations from expected behavior under large applied loads.[38,73] By avoiding the small-angle approximation, the geodesic approach showed close agreement even under large applied loads when compared with accurate yet computationally expensive dynamical simulations, whereas the spline-based approach exhibited systematically smaller deformations compared to the dynamical solution. This systematic error may also be partly explained by examining the $\hat{s}$-profiles of the strain components in the various models, as discussed in the Supporting Information, section 1.4.

One practical concern in implementing the various functional forms introduced here is the associated computational cost of evaluating the filament position and energy and of numerically minimizing the energy. A related issue of these models is their locality, or the dependence of local quantities on either only "nearby" parameters of the model rather than on almost all parameters of the model. For instance, in the spline-based models smoothness is enforced by relating the control points of later segments to those of earlier segments. This causes the expression for the position on segment i to depend on all parameters up to that segment, so that the complexity of the model grows faster than linearly with the number of knot points. It should be possible to use B-splines to alleviate this nonlocality in future developments.[59,60] Nonlocality is more inherent in the geodesic model, arising from the expression of the backbone curve $r(\hat{s})$ as an integral up to $\hat{s}$ of the tangent $d\mathbf{r}/d\hat{s}$. While closed form solutions for this integral are straightforwardly obtained (see the Supporting Information), there is no way to avoid this dependence of the position on segment i on the parameters up to segment i. However, measurements of the time taken to evaluate the energy function as N_k is varied for each model show that the geodesic models can be more computationally efficient than the spline-based model, as discussed in the Supporting Information, section 1.3.

Various extensions to the models presented here are possible. For the spline-based models, it was mentioned that

B-splines may be used to improve locality, and exponential splines could also be used to increase expressivity by allowing for both polynomial and exponential contributions to the filament functional form.[59−61] One could also mix the geodesic and spline-based approaches. For instance, in the geodesic models one can relax the constraint that the components $\zeta_\alpha(\hat{s})$ of $d\mathbf{r}/d\hat{s}$ are constant on the segments; $\zeta_\alpha(\hat{s})$ could instead be a spline function in $\hat{s}$ on the segment and the energy terms involving $\zeta_\alpha(\hat{s})$ could still be found exactly (see the Supporting Information, section 2.2). Other functional forms not considered here could also be investigated. Rather than using splines to parametrize the Euler angles of Q, splines could be used to parametrize curves of quaternions or other representations for Q.[74] In principle one could also allow the knot coordinates $\hat{s}_i$ to become free model parameters, so that the segment lengths are adjustable during minimization. Additionally, one may use the functional forms presented here but adopt a dynamical, rather than variational, approach to study filament mechanics. Considering the free model parameters of these functional forms to be generalized mechanical coordinates, one could derive equations of motion giving the time evolution of the filament's configuration using Hamiltonian or Langevin dynamics.[75,76] This can offer a way to endow a filament with all mechanical degrees of freedom of the Cosserat model in time integration-based simulations of semiflexible polymer networks, while preserving the computational efficiency of tracking only a handful of free model parameters.[15−17] Finally, our work is based on the Cosserat theory of elastic rods which is more general than the Kirchoff theory, but less general than the theory of Green and Naghdi which allows in-plane shearing of the rod's cross sections.[77,78] Accommodating in-plane shearing deformations considerably complicates the mathematics by introducing nonorthogonal local directors, and we expect that it contributes only minor corrections to the dynamics of filaments like actin. However, future works may apply this more general approach to study biopolymer mechanics.

In this paper, we have considered a coarse-grained representation of an actin filament which has a constant circular cross-section and lacks monomer-level resolution. In the accompanying paper, ref 1, we describe a finer-grained monomer-level model of an actin filament that preserves the helical filament microstructure, and we develop a method for smoothly connecting the monomeric model to the constant cross-section model presented here. This multiresolution modeling approach allows for fine control over the trade-off between biological detail and computational expense. In ref 1 we also discuss in detail issues of parametrization, which was treated only briefly here (see Supporting Information, section 2.1), as well as validations of these models using direct comparison to experimental measurements of actin filament configurations. Therefore, while some important chemical detail has been omitted in the present paper, we discuss in ref 1 how this detail can be built back into the model in a systematic manner.

An exciting future application of efficient computational models of finite-width filaments will be to investigate emergent chiral symmetry breaking in active, self-organizing cytoskeletal networks. Our simulation of a chiral filament bundle can be viewed as a preliminary investigation into this topic, showing that chirality in the mechanical compliance of individual finite-width filaments (as encoded in the parameter $C_{3,3}$) can give rise through surface-bound cross-linkers to chiral rotation of a

multifilament bundle. Other mechanisms by which broken chiral symmetry can propagate to larger spatial scales may be studied in more complete simulations of motorized cytoskeletal networks, for instance using the new version of MEDYAN augmented to use a Cosserat model for filaments, which was presented in this paper.[18] In addition, such network-level simulations could explore the effect of cofilin on cytoskeletal dynamics. It has been shown that cofilin molecules bind cooperatively to actin filaments and induce a torsional strain that leads to filament severing.[73,79] This nontrivial mechanical effect could be realistically accounted for in simulation using the finite-width models presented here.

■ ASSOCIATED CONTENT

Ⓢⓘ Supporting Information

The Supporting Information is available free of charge at https://pubs.acs.org/doi/10.1021/acs.jctc.2c00318.

> Supplementary results: description of Euler buckling study, description of test cases, comparison of timing and accuracy of models, profiles of strain functions. Supplementary methods: parametrization details, deriving expressions for $Q(\hat{s})$ and $r(\hat{s})$ in the geodesic models, deriving expressions for energy functions in the geodesic models, implementing the geodesic models in MEDYAN (PDF)

■ AUTHOR INFORMATION

Corresponding Authors

Radek Erban − *Mathematical Institute, University of Oxford, Oxford OX2 6GG, United Kingdom;* ⓞ orcid.org/0000-0001-8470-3763; Email: erban@maths.ox.ac.uk

Garegin A. Papoian − *Department of Chemistry & Biochemistry, Institute for Physical Science and Technology, University of Maryland, College Park, Maryland 20742, United States;* ⓞ orcid.org/0000-0001-8580-3790; Email: gpapoian@umd.edu

Authors

Carlos Floyd − *Department of Chemistry & Biochemistry, Institute for Physical Science and Technology, University of Maryland, College Park, Maryland 20742, United States;* ⓞ orcid.org/0000-0002-6270-7250

Haoran Ni − *Department of Chemistry & Biochemistry, Institute for Physical Science and Technology, University of Maryland, College Park, Maryland 20742, United States;* ⓞ orcid.org/0000-0003-3600-4583

Ravinda S. Gunaratne − *Mathematical Institute, University of Oxford, Oxford OX2 6GG, United Kingdom;* ⓞ orcid.org/0000-0002-9108-1816

Complete contact information is available at:
https://pubs.acs.org/10.1021/acs.jctc.2c00318

Notes

The authors declare no competing financial interest.

■ REFERENCES

(1) Gunaratne, R.; Floyd, C.; Ni, H.; Papoian, G. A.; Erban, R. On Stretching, Bending, Shearing and Twisting of Actin Filaments II: Multi-Resolution Modelling. *arXiv* **2022**, No. 01284, DOI: 10.48550/arXiv.2203.01284.

(2) Fletcher, D. A.; Mullins, R. D. Cell mechanics and the cytoskeleton. *Nature* **2010**, *463*, 485−492.

(3) Howard, J., et al. *Mechanics of motor proteins and the cytoskeleton*; Oxford University Press, 2001.

(4) McCullagh, M.; Saunders, M. G.; Voth, G. A. Unraveling the mystery of ATP hydrolysis in actin filaments. *J. Am. Chem. Soc.* **2014**, *136*, 13053−13058.

(5) Belmont, L. D.; Orlova, A.; Drubin, D. G.; Egelman, E. H. A change in actin conformation associated with filament instability after Pi release. *Proc. Natl. Acad. Sci. U. S. A.* **1999**, *96*, 29−34.

(6) Mani, S.; Katkar, H. H.; Voth, G. A. Compressive and Tensile Deformations Alter ATP Hydrolysis and Phosphate Release Rates in Actin Filaments. *J. Chem. Theory Comput.* **2021**, *17*, 1900−1913.

(7) Mizuno, D.; Tardin, C.; Schmidt, C. F.; MacKintosh, F. C. Nonequilibrium mechanics of active cytoskeletal networks. *Science* **2007**, *315*, 370−373.

(8) Cordes, A.; Witt, H.; Gallemí-Pérez, A.; Brückner, B.; Grimm, F.; Vache, M.; Oswald, T.; Bodenschatz, J.; Flormann, D.; Lautenschläger, F.; et al. Prestress and area compressibility of actin cortices determine the viscoelastic response of living cells. *Phys. Rev. Lett.* **2020**, *125*, 068101.

(9) Gardel, M.; Shin, J. H.; MacKintosh, F.; Mahadevan, L.; Matsudaira, P.; Weitz, D. A. Elastic behavior of cross-linked and bundled actin networks. *Science* **2004**, *304*, 1301−1305.

(10) Ajeti, V.; Tabatabai, A. P.; Fleszar, A. J.; Staddon, M. F.; Seara, D. S.; Suarez, C.; Yousafzai, M. S.; Bi, D.; Kovar, D. R.; Banerjee, S.; et al. Wound healing coordinates actin architectures to regulate mechanical work. *Nat. Phys.* **2019**, *15*, 696−705.

(11) Floyd, C.; Papoian, G. A.; Jarzynski, C. Quantifying dissipation in actomyosin networks. *Interface focus* **2019**, *9*, 20180078.

(12) Yamaoka, H.; Matsushita, S.; Shimada, Y.; Adachi, T. Multiscale modeling and mechanics of filamentous actin cytoskeleton. *Biomechanics and modeling in mechanobiology* **2012**, *11*, 291−302.

(13) Broedersz, C. P.; MacKintosh, F. C. Modeling semiflexible polymer networks. *Rev. Mod. Phys.* **2014**, *86*, 995.

(14) Rubinstein, M.; Colby, R. H., et al. *Polymer physics*; Oxford university press: New York, 2003; Vol. 23.

(15) Freedman, S. L.; Banerjee, S.; Hocky, G. M.; Dinner, A. R. A versatile framework for simulating the dynamic mechanical structure of cytoskeletal networks. *Biophysical journal* **2017**, *113*, 448−460.

(16) Nedelec, F.; Foethke, D. Collective Langevin dynamics of flexible cytoskeletal fibers. *New J. Phys.* **2007**, *9*, 427.

(17) Kim, T.; Hwang, W.; Lee, H.; Kamm, R. D. Computational analysis of viscoelastic properties of crosslinked actin networks. *PLoS Comput. Biol.* **2009**, *5*, No. e1000439.

(18) Popov, K.; Komianos, J.; Papoian, G. A. MEDYAN: Mechanochemical simulations of contraction and polarity alignment in actomyosin networks. *PLoS computational biology* **2016**, *12*, No. e1004877.

(19) Floyd, C.; Chandresekaran, A.; Ni, H.; Ni, Q.; Papoian, G. A. Segmental Lennard-Jones interactions for semi-flexible polymer networks. *Mol. Phys.* **2021**, *119*, No. e1910358.

(20) Tee, Y. H.; Shemesh, T.; Thiagarajan, V.; Hariadi, R. F.; Anderson, K. L.; Page, C.; Volkmann, N.; Hanein, D.; Sivaramakrishnan, S.; Kozlov, M. M.; et al. Cellular chirality arising from the self-organization of the actin cytoskeleton. *Nature cell biology* **2015**, *17*, 445−457.

(21) Schaller, V.; Weber, C.; Semmrich, C.; Frey, E.; Bausch, A. R. Polar patterns of driven filaments. *Nature* **2010**, *467*, 73−77.

(22) Fritzsche, M.; Li, D.; Colin-York, H.; Chang, V.; Moeendarbary, E.; Felce, J.; Sezgin, E.; Charras, G.; Betzig, E.; Eggeling, C. Self-organizing actin patterns shape membrane architecture but not cell mechanics. *Nat. Commun.* **2017**, *8*, 1−14.

(23) Egelman, E.; Francis, N.; DeRosier, D. F-actin is a helix with a random variable twist. *Nature* **1982**, *298*, 131−135.

(24) De La Cruz, E. M.; Gardel, M. L. Actin mechanics and fragmentation. *J. Biol. Chem.* **2015**, *290*, 17137−17144.

(25) Beausang, J. F.; Schroeder, H. W., 3rd; Nelson, P. C.; Goldman, Y. E. Twirling of actin by myosins II and V observed via polarized TIRF in a modified gliding assay. *Biophysical journal* **2008**, *95*, 5820−5831.

(26) Vilfan, A. Twirling motion of actin filaments in gliding assays with nonprocessive myosin motors. *Biophysical journal* **2009**, *97*, 1130−1137.

(27) Naganathan, S. R.; Fürthauer, S.; Nishikawa, M.; Jülicher, F.; Grill, S. W. Active torque generation by the actomyosin cell cortex drives left−right symmetry breaking. *elife* **2014**, *3*, No. e04165.

(28) Naganathan, S. R.; Middelkoop, T. C.; Fürthauer, S.; Grill, S. W. Actomyosin-driven left-right asymmetry: from molecular torques to chiral self organization. *Curr. Opin. Cell Biol.* **2016**, *38*, 24−30.

(29) Ma, R.; Berro, J. Structural organization and energy storage in crosslinked actin assemblies. *PLoS computational biology* **2018**, *14*, No. e1006150.

(30) De La Cruz, E. M.; Roland, J.; McCullough, B. R.; Blanchoin, L.; Martiel, J. L. Origin of twist-bend coupling in actin filaments. *Biophys. J.* **2010**, *99*, 1852−1860.

(31) Yamaoka, H.; Adachi, T. Coupling between axial stretch and bending/twisting deformation of actin filaments caused by a mismatched centroid from the center axis. *International Journal of Mechanical Sciences* **2010**, *52*, 329−333.

(32) Cyron, C. J.; Müller, K. W.; Bausch, A. R.; Wall, W. A. Micromechanical simulations of biopolymer networks with finite elements. *J. Comput. Phys.* **2013**, *244*, 236−251.

(33) Müller, K. W.; Meier, C.; Wall, W. A. Resolution of sub-element length scales in Brownian dynamics simulations of biopolymer networks with geometrically exact beam finite elements. *J. Comput. Phys.* **2015**, *303*, 185−202.

(34) Carrega, J.-C. *Théorie des corps*; A. Hermann et fils, 1981.

(35) Rubin, M. *Cosserat Theories: Shells, Rods and Points*; Springer, 2000.

(36) Gazzola, M.; Dudte, L.; McCormick, A.; Mahadevan, L. *Forward and inverse problems in the mechanics of soft filaments*; Royal Society Open Science, 2018, *5*, 171628.

(37) Antman, S. *Nonlinear Problems of Elasticity. Applied Mathematical Sciences*, 2nd ed.; Springer: New York, 2005; Vol. 107, p 1.

(38) O'Reilly, O. M. *Modeling Nonlinear Problems in the Mechanics of Strings and Rods*; Springer, 2017.

(39) Kirchhoff, G. Ueber das Gleichgewicht und die Bewegung eines unendlich dünnen elastischen Stabes. *Journal für die reine und angewandte Mathematik* **1859**, *1859*, 285−313.

(40) Dill, E. H. Kirchhoff's theory of rods. *Archive for History of Exact Sciences* **1992**, *44*, 1−23.

(41) Bergou, M.; Wardetzky, M.; Robinson, S.; Audoly, B.; Grinspun, B. ACM SIGGRAPH ASIA 2008 Courses. *Proceedings of SIGGRAPH Asia'08*; Association for Computing Machinery, 2008; pp 1−12.

(42) Zhang, X.; Chan, F. K.; Parthasarathy, T.; Gazzola, M. Modeling and simulation of complex dynamic musculoskeletal architectures. *Nat. Commun.* **2019**, *10*, 4825.

(43) Cohen, H.; Desilva, C. N. Nonlinear theory of elastic directed surfaces. *Journal of Mathematical Physics* **1966**, *7*, 960−966.

(44) Kreyszig, E. *Introduction to differential geometry and Riemannian geometry*; University of Toronto Press, 1968.

(45) Healey, T. Material symmetry and chirality in nonlinearly elastic rods. *Mathematics and Mechanics of Solids* **2002**, *7*, 405−420.

(46) Smith, M. L.; Healey, T. J. Predicting the onset of DNA supercoiling using a non-linear hemitropic elastic rod. *International Journal of Non-Linear Mechanics* **2008**, *43*, 1020−1028.

(47) Spillmann, J.; Teschner, M. CORDE: Cosserat rod elements for the dynamic simulation of one-dimensional elastic objects. *Symposium on Computer Animation 2007 - ACM SIGGRAPH/Eurographics Symposium Proceedings, SCA 2007*; Association for Computing Machinery, 2007; pp 63−72.

(48) Baras, F.; Mansour, M. M. Reaction-diffusion master equation: A comparison with microscopic simulations. *Phys. Rev. E* **1996**, *54*, 6139.

(49) Floyd, C.; Papoian, G. A.; Jarzynski, C. Gibbs free energy change of a discrete chemical reaction event. *J. Chem. Phys.* **2020**, *152*, 084116.

(50) MacKintosh, F. C.; Schmidt, C. F. Active cellular materials. *Curr. Opin. Cell Biol.* **2010**, *22*, 29−35.

(51) Chandrasekaran, A.; Upadhyaya, A.; Papoian, G. A. Remarkable structural transformations of actin bundles are driven by their initial polarity, motor activity, crosslinking, and filament treadmilling. *PLoS computational biology* **2019**, *15*, No. e1007156.

(52) Komianos, J. E.; Papoian, G. A. Stochastic ratcheting on a funneled energy landscape is necessary for highly efficient contractility of actomyosin force dipoles. *Physical Review X* **2018**, *8*, 021006.

(53) Ni, Q.; Papoian, G. A. Turnover versus treadmilling in actin network assembly and remodeling. *Cytoskeleton* **2019**, *76*, 562.

(54) Li, X.; Ni, Q.; He, X.; Kong, J.; Lim, S.-M.; Papoian, G. A.; Trzeciakowski, J. P.; Trache, A.; Jiang, Y. Tensile Force Induced Cytoskeletal Reorganization: Mechanics Before Chemistry. *BioRxiv* **2020**, No. 1007693.

(55) Ni, H.; Papoian, G. A. Membrane-medyan: Simulating deformable vesicles containing complex cytoskeletal networks. *bioRxiv* **2021**, No. 436229.

(56) Floyd, C.; Levine, H.; Jarzynski, C.; Papoian, G. A. Understanding cytoskeletal avalanches using mechanical stability analysis. *Proc. Natl. Acad. Sci. U. S. A.* **2021**, *118*.

(57) MacDonald, J. K. Successive approximations by the Rayleigh-Ritz variation method. *Phys. Rev.* **1933**, *43*, 830−833.

(58) Slaughter, W. S. *North-Holland Series in Applied Mathematics and Mechanics*; Springer Science & Business Media, 1973; Vol. 16, pp 46−78.

(59) Shikin, E. V.; Plis, A. I. *Handbook on Splines for the User*; CRC press, 1995.

(60) Prautzsch, H.; Boehm, W.; Paluszny, M. *Bézier and B-spline techniques*; Springer Science & Business Media, 2002.

(61) Späth, H. Exponential spline interpolation. *Computing* **1969**, *4*, 225−233.

(62) Neuman, E. Uniform approximation by some Hermite interpolating splines. *Journal of Computational and Applied Mathematics* **1978**, *4*, 7−9.

(63) O'Reilly, O. M. *Intermediate dynamics for engineers: a unified treatment of Newton-Euler and Lagrangian mechanics*; Cambridge University Press Cambridge, 2008.

(64) *Mathematica*, ver. 12.2; Wolfram: Champaign, IL, 2020.

(65) Jeevanjee, N. *An introduction to tensors and group theory for physicists*; Springer, 2011.

(66) Huynh, D. Q. Metrics for 3D rotations: Comparison and analysis. *Journal of Mathematical Imaging and Vision* **2009**, *35*, 155−164.

(67) Park, F. C. Distance metrics on the rigid-body motions with applications to mechanism design. *J. Mech. Des.* **1995**, 10.1148.

(68) Park, F. C.; Ravani, B. Smooth invariant interpolation of rotations. *ACM Transactions on Graphics (TOG)* **1997**, *16*, 277−295.

(69) Tojkander, S.; Gateva, G.; Lappalainen, P. Actin stress fibers−assembly, dynamics and biological roles. *Journal of cell science* **2012**, *125*, 1855−1864.

(70) Goley, E. D.; Welch, M. D. The ARP2/3 complex: an actin nucleator comes of age. *Nat. Rev. Mol. Cell Biol.* **2006**, *7*, 713−726.

(71) Binney, J. J.; Dowrick, N. J.; Fisher, A. J.; Newman, M. E. *The theory of critical phenomena: an introduction to the renormalization group*; Oxford University Press, 1992.

(72) Linsmeier, I.; Banerjee, S.; Oakes, P. W.; Jung, W.; Kim, T.; Murrell, M. P. Disordered actomyosin networks are sufficient to produce cooperative and telescopic contractility. *Nat. Commun.* **2016**, *7*, 1−9.

(73) De La Cruz, E. M. How cofilin severs an actin filament. *Biophysical reviews* **2009**, *1*, 51−59.

(74) Altmann, S. L. *Rotations, quaternions, and double groups*; Courier Corporation, 2005.

(75) Goldstein, H.; Poole, C.; Safko, J. *Classical mechanics*; Pearson, 2002.

(76) Risken, H. *The Fokker-Planck Equation*; Springer, 1996; pp 63−95.

(77) Green, A. E.; Laws, N. A general theory of rods. *Proceedings of the Royal Society of London. Series A. Mathematical and Physical Sciences* **1966**, *293*, 145−155.

(78) Green, A.; Naghdi, P. A unified procedure for construction of theories of deformable media. II. Generalized continua. *Proceedings of the Royal Society of London. Series A: Mathematical and Physical Sciences* **1995**, *448*, 357−377.

(79) McCullough, B. R.; Grintsevich, E. E.; Chen, C. K.; Kang, H.; Hutchison, A. L.; Henn, A.; Cao, W.; Suarez, C.; Martiel, J.-L.; Blanchoin, L.; et al. Cofilin-linked changes in actin filament flexibility promote severing. *Biophysical journal* **2011**, *101*, 151−159.

📖 Recommended by ACS

Structural Design of CANs with Fine-Tunable Relaxation Properties: A Theoretical Framework Based on Network Structure and Kinetics Modeling

Osman Konuray, Xavier Ramis, *et al.*

JUNE 23, 2023
MACROMOLECULES

READ 🗗

Origins of the Failure of the Activity Virial Series

David A. Kofke.

APRIL 14, 2023
THE JOURNAL OF PHYSICAL CHEMISTRY B

READ 🗗

Siloxane Molecules: Nonlinear Elastic Behavior and Fracture Characteristics

Tianchi Li, Stefanie Heyden, *et al.*

FEBRUARY 08, 2023
MACROMOLECULES

READ 🗗

Probabilistic Approach to Low Strain Rate Atomistic Simulations of Ultimate Tensile Strength of Polymer Crystals

José Cobeña-Reyes, Ashlie Martini, *et al.*

AUGUST 29, 2023
JOURNAL OF CHEMICAL THEORY AND COMPUTATION

READ 🗗

Get More Suggestions >